Materials Chemistry and Physics 317 (2024) 129184

Contents lists available at ScienceDirect

Materials Chemistry and Physics

journal homepage: www.elsevier.com/locate/matchemphys

Cobalt-doped SnS_2 nanoplates for high-efficiency catalysis applications

Qais M. Al-Bataineh [a,b,*], A.B. Migdadi [c,1], Ahmad A. Ahmad [c], Oana Brincoveanu [d,e], Alexandra Mocanu [d,f], Gabriela Toader [g], Ahmad D. Telfah [h,i]

[a] Leibniz Institut für Analytische Wissenschaften-ISAS-e.V., Bunsen-Kirchhoff-Straße 11, 44139, Dortmund, Germany
[b] Experimental Physics, T.U. Dortmund University, 44227, Dortmund, Germany
[c] Department of Physical Sciences, Faculty of Science and Arts, Jordan University of Science & Technology, P.O. Box 3030, Irbid, 22110, Jordan
[d] National Institute for Research and Development in Microtechnologies – IMT Bucharest, 126A Erou Iancu Nicolae Street, 077190, Bucharest, Romania
[e] Research Institute of the University of Bucharest, ICUB Bucharest, Soseaua Panduri, nr. 90, Sector 5, 050663, București, Romania
[f] University Politehnica of Bucharest, Faculty of Chemical Engineering and Biotechnologies, 1- 7 Gh. Polizu Street, 011061, Bucharest, Romania
[g] Military Technical Academy "Ferdinand I ", 39-49 George Cosbuc Av., 050141, Bucharest, Romania
[h] Nanotechnology Center, The University of Jordan, 11942, Amman, Jordan
[i] Department of Physics, University of Nebraska at Omaha, Omaha, NE, 68182, USA

HIGHLIGHTS

- The photocatalytic degradation of MIT in water was successfully performed using Co–SnS_2 nanoplates under UV irradiation.
- Pure SnS_2 and Co–SnS_2 nanoplates were synthesized using a hydrothermal method at 180 °C.
- X-ray diffraction patterns (XRD) show that the crystallite size of nanoplates increases from 26 nm to 48 nm.
- Pure SnS_2 nanoplates exhibit plate-like nanostructure with smooth surfaces.
- The degradation efficiency of MIT using SnS_2 and Co–SnS_2 nanoplates after 160 min is 66% and 91%, respectively.

ARTICLE INFO

Keywords:
Cobalt doped tin sulfide (Co–SnS_2) nanoplates
Methylisothiazolinone (MIT)
Photocatalytic degradation process
Optical band structure
Electrical conductivity

ABSTRACT

The photocatalysis degradation of methyl iso thiazolinone (MIT) in water was effectively performed using cobalt-doped tin sulfide (Co–SnS_2) nanoplates under UV irradiation. X-ray diffraction patterns (XRD) show that the crystallite size of nanoplates increases from 26 nm to 48 nm. Undoped SnS_2 nanoplates exhibit plate-like nanostructure with smooth surfaces, with a size of 150–400 μm and a 50–70 nm thickness. Doping SnS_2 nanoplates with cobalt increases the nanoplate's size to 300–600 nm. SnS_2 and Co-doped SnS_2 nanoplates have indirect bandgap energy with values of 1.95 and 1.86 eV, respectively. On the other hand, the electrical conductivity of SnS_2 and Co-doped SnS_2 nanoplates was 1.67×10^{-5} S.cm^{-1} and 1.64×10^{-4} S.cm^{-1}, which increases to 6.54×10^{-4} S.cm^{-1} and 1.25×10^{-2} S.cm^{-1} upon UV irradiation, respectively. The higher degradation efficiency of a 5 mg/L concentration of MIT via SnS_2 and Co–SnS_2 nanoplates after 160 min is 66% and 91%, respectively. Finally, the photodegradation process was investigated using UV-VIS and FTIR analysis.

1. Introduction

Water pollution has become a severe problem with increased industrial development, causing many health hazards [1]. Photocatalysis has been considered a promising, efficient, and green method to treat and decompose organic pollutants in water [2–4]. Degrading water via the photocatalyst process to semiconducting materials reveals less energy usage and creates a couple of holes and electrons due to light exposure. The couples of electrons and holes are caused to sink to the over-layered surface, leaving behind ionic species such as oxygen and hydroxyl and free holes (O_2^{-*}, OH^*, and h^+). This process decomposes the contents of the organics into carbon oxides and water (CO_2 and H_2O) through an oxidizing and reducing process [5,6].

Methyl isothiazolinone (2-methyl-4-isothiazolin-3-one) (MIT) is

* Corresponding author. Leibniz Institut für Analytische Wissenschaften-ISAS-e.V., Bunsen-Kirchhoff-Straße 11, 44139, Dortmund, Germany
E-mail address: qais.albataineh@tu-dortmund.de (Q.M. Al-Bataineh).
[1] Equal contribution to the first author.

https://doi.org/10.1016/j.matchemphys.2024.129184
Received 19 January 2024; Received in revised form 18 February 2024; Accepted 10 March 2024
Available online 14 March 2024

generally known as a biocide for cleaning agents, cosmetics, reverse osmosis, paints, and coatings due to its high antibacterial activity [7]. However, MIT is a potent skin irritant that can cause allergic responses [8,9]. Limited works have explored the MIT degrading process biologically or in photocatalysis handling [10–13]. However, degradation studies of MIT by the oxidation mechanism are rare due to increasing toxicity caused by chemical addition, high energy consumption, and difficulty in catalyst recovery. Therefore, economical and harmless techniques must be established for handling MIT.

Among all metal sulfides, tin sulfide (SnS_2) is a low bandgap semiconductor (2–2.4 eV). It has negative charge carriers [14], which provides a high catalytic activity for organic pollutants [15,16] since SnS_2 has a narrow indirect bandgap and high quantum yield [17]. Additionally, SnS_2 is commonly used in various ways in technology, such as optoelectronics [18], gas sensing [19], solar cells [20], and energy storage devices [21]. SnS_2 nanoplates are 2D trigonal crystal di-chalcogenides with layers [22,23]. They have unique optoelectronic characteristics, flat surfaces, and poor carrier recombination, enabling photocatalytic reactivity [24,25]. The physical properties of SnS_2, including the catalytic characteristics, can be manipulated by doping it with transition metals [26–28].

Among all transition metals, cobalt (Co) is a dopant in SnS_2 nanoplates owing to the excess electrons and the significant solubility [29]. Additionally, the ionic radius of cobalt (200 p.m.) is comparable to that of tin (225 p.m.), leading to the exchange of the Sn^{+2} ions in the nanoplates by Co^{2+} ions. Due to the non-full d orbitals, Co^{2+} ions trap electrons in the SnS_2 nanoplates, enhancing the photocatalytic activity [30].

As mentioned above, limited works have explored the MIT degrading process through the photocatalysis mechanism. Therefore, we proposed an innovative method of creating sulfur vacancies modified SnS_2 nanoplates with high photogenerated carriers and more adjective reaction sites through cobalt doping (Co^{2+}), which consequently enhances the photocatalysis efficiency for MIT degradation. Co-doped SnS_2 nanoplates are accomplished by exchanging the Sn sites by Co with introducing sulfur vacancies, which provides high photocatalytic efficiency compared to SnS_2 nanoplates [28]. In particular, undoped SnS_2 and Co-doped SnS_2 nanoplates were prepared hydrothermally. Additionally, the physical properties, including crystal structure, elemental structure, morphology, bandgap energy, electrical conductivity, and photoconductivity, were correlated with the changes in bandgap structure and photoconductivity as a consequence of using Co as a doping agent for the SnS_2 nanoplates. Therefore, the photodegradation process of MIT investigated the photocatalytic performance of undoped SnS_2 and Co-doped SnS_2 nanoplates.

2. Methods

2.1. Synthesis

A hydrothermal process was used to synthesize undoped SnS_2 and cobalt-doped SnS_2 (Co–SnS_2) nanoplates. All chemical used in this work was purchased from Sigma Aldrich without further purification. For synthesized undoped SnS_2 nanoplates, 1.40 g of tin chloride pentahydrate ($SnCl_4.5H_2O$) (1 mM) and 1.52 g of thiourea (CH_4N_2S) (5 mM) were dissolved in 60 mL of distilled water under continuous stirring for 1 h at room temperature. On the other hand, for the synthesis of Co–SnS_2 nanoplates (5 wt%), 1.40 g of tin chloride pentahydrate ($SnCl_4.5H_2O$), 0.07 g of cobalt acetate ($C_4H_6CoO_4$), and 1.52 g of thiourea (CH_4N_2S) (5 mM) were dissolved in 60 mL of deionized distilled water while kept on the stirrer for one at standard conditions. Consequently, the two solutions were transferred separately into an autoclave at 180 °C for 24 h. The nanoplates were collected and washed with water and ethanol. Finally, the resultant nanoplates were dried at 80 °C overnight until constant mass. The overall synthesis process of undoped SnS_2 and Co–SnS_2 nanoplates is schematically presented in (Supplementary file, Figure S1a).

2.2. Characterizations

The crystal structure of pure SnS_2 and Co–SnS_2 nanoplates was investigated using powder X-ray diffraction (XRD, Malvern Panalytical Ltd.) by CuKα_1 ray ($\lambda = 0.1540598$ nm) in angles range of 10°–50° with a step of 0.02°. The nanoplates morphology and size were investigated using a scanning electron microscope (SEM, Nova NanoSEM 630, FEI Company) using an accelerating voltage of 10 kV. The elemental distribution of pure SnS_2 and Co–SnS_2 nanoplates was performed with the element energy dispersive spectroscopy (EDX) system (Smart Insight AMETEK). The EDX map was acquired at an acceleration voltage of 10 kV, with a working distance of 5 mm and 20 μm magnification. Fourier transform infrared spectroscopy (FTIR, Bruker VERTEX 80/80v) in the spectral range of 400–4000 cm^{-1} was used to investigate the chemical structure of the nanoplates. Pure SnS_2 and Co–SnS_2 nanoplates were dispersed in distilled water using an ultrasonication probe for 10 min. After that, the pure SnS_2 and Co–SnS_2 nanoplates were coated on the ITO glass substrates (250 nm ITO on glass) using the casting method by dropping equal amounts on 1 cm^2 of ITO glass substrate and dried them at 80 °C overnight. Optical properties of coated pure SnS_2 and Co–SnS_2 nanoplates were investigated using a UV–Vis spectrophotometer (U–3900H), whereas the electrical conductivity maps were measured using a 4-point probe station (Microworld Inc.).

2.3. Photocatalytic degradation experiments

The photocatalytic degradation of MIT was performed using 50 mg/L of pure SnS_2 and Co–SnS_2 nanoplates with different concentrations of MIT (5, 10, 15, and 20 mg/L). First, four amounts of MIT (5, 10, 15, 20 mg) were dissolved in 1.0 L deionized water in the dark overnight. After that, each 1.0 L of MIT solution was divided into two amounts (500 mL). 25 mg of pure SnS_2 and Co–SnS_2 nanoplates was added into the four concentrations under continuous stirring for 1 h. The solutions were irradiated by UV light (260 nm, 16 W) under constant stirring (500 rpm) with an adjustable distance of about 10 cm (Figure S1b). 5 mL of each solution was taken to a centrifugation tube after irradiation times of 0, 10, 20, 30, 45, 60, 90, 120, and 160 min. After that, the nanoparticles were separated from the tubes using a centrifuge system to investigate the degradation process of MIT. All photocatalytic experiments were performed at room temperature, controlled using a water bath to avoid increasing the temperature during the degradation reaction. UV–Vis spectrophotometric (U–3900H) and Fourier transform infrared spectroscopy (FTIR) (Bruker Tensor 27 spectrometer) were used to investigate the degradation process of MIT.

3. Results and discussion

3.1. SnS_2 and Co–SnS_2 nanoplates characterizations

Photocatalyst pure SnS_2 and Co–SnS_2 nanoplates were synthesized using a hydrothermal method, using a 1:5 stoichiometric mixture of $SnCl_4.5H_2O$ and $C_4H_6CoO_4$ as a source of Sn and Co in addition to thiourea as a source of S at 180 °C. According to I. Shown et al. [31], thiourea enhances the anisotropic growth of SnS_2 and Co–SnS_2 nanoplates. The morphology of pure SnS_2 and Co–SnS_2 nanoplates was studied using a scanning electron microscope (SEM). Fig. 1 illustrates the typical SEM micrographs of pure SnS_2 and Co–SnS_2 nanoplates. Pure SnS_2 nanoplates exhibit plate-like nanostructure with smooth surfaces, where the nanoplates have a size of 150–400 μm and thickness of 50–70 nm (Fig. 1a). Doping SnS_2 nanoplates with cobalt increases the nanoplates size to 300–600 nm (Fig. 1b).

The elemental and chemical structure of pure SnS_2 and Co–SnS_2 nanoplates were investigated using EDX and FTIR spectroscopies. EDX elemental maps for pure SnS_2 and Co–SnS_2 nanoplates are depicted in

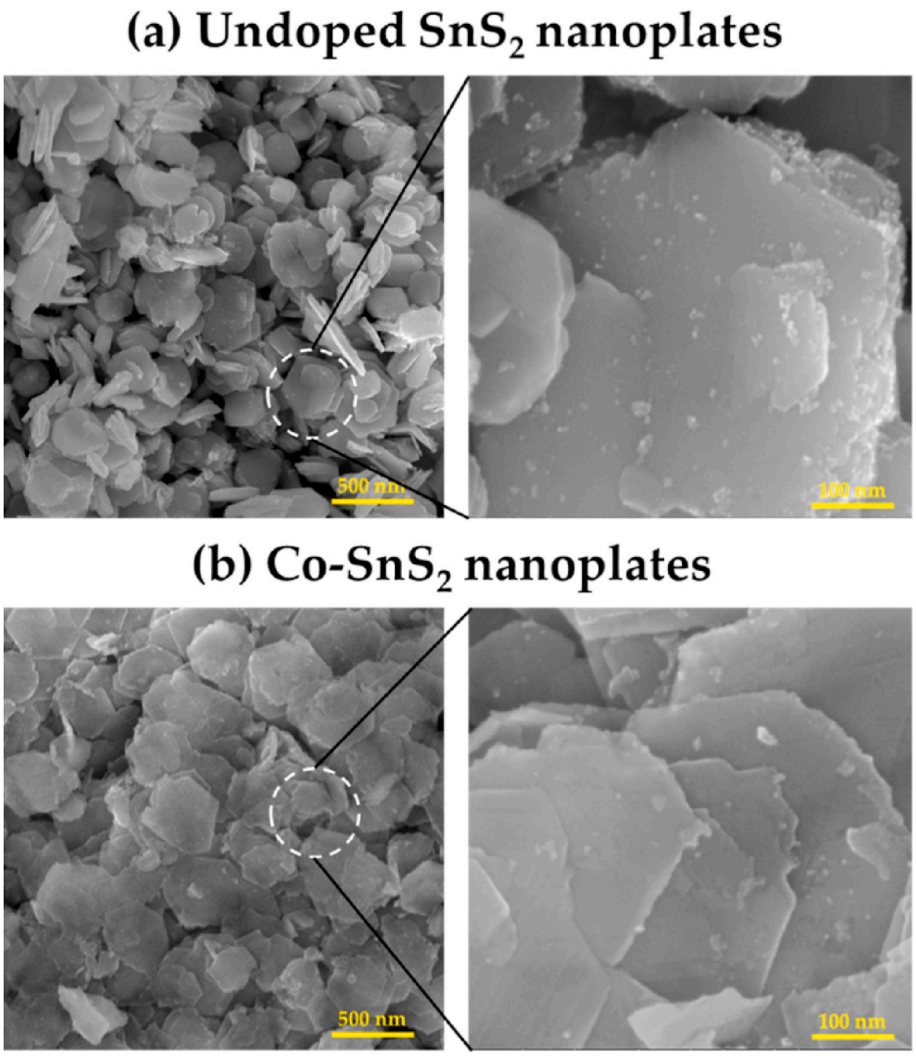

Fig. 1. Morphological properties of SnS_2 and Co–SnS_2 nanoplates. (a) SEM micrographs of undoped SnS_2 nanoplates, and (b) SEM micrographs of Co–SnS_2 nanoplates at 500 nm and 100 nm scale, respectively.

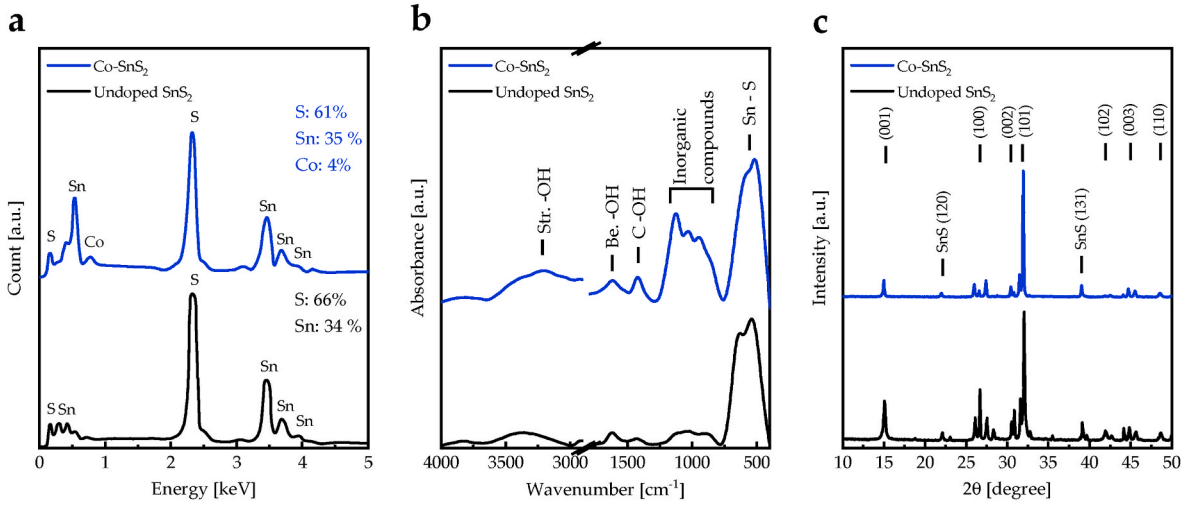

Fig. 2. Elements, chemical, and crystalline characteristics of SnS_2 and Co–SnS_2 nanoplates. (a) EDX scans of SnS_2 and Co–SnS_2 nanoplates. (b) FTIR spectra of undoped SnS_2 and Co–SnS_2 nanoplates. (c) XRD configurations of SnS_2 and Co–SnS_2 nanoplates.

Supplementary file Figures S2a and S2b. The EDX elemental maps shows that Sn, S, and Co are distributed homogeneously within the nanoplates. The elemental analysis for pure SnS_2 and Co–SnS_2 nanoplates was performed by EDX spectra (Fig. 2a). The S to Sn atomic ratio is about 1.94 and 1.74 for pure SnS_2 and Co–SnS_2 nanoplates, respectively. Additionally, Co–SnS_2 nanoplates contain a cobalt atomic ratio of about 4%, confirming the successful incorporation of Co with SnS_2 nanoplates. Fig. 2b illustrates the FTIR spectra of pure SnS_2 and Co–SnS_2 nanoplates. Both pure SnS_2 and Co–SnS_2 nanoplates exhibit the typical vibrational bands of SnS_2, i.e., stretching OH (~3360 cm^{-1}), bending OH (~1627 cm^{-1}), C–OH (~1434 cm^{-1}), and Sn–S (500-600 cm^{-1}) [32]. Stretching and bending OH bonds have been aroused from the surface hydroxyls and adsorbed water [33]. Additionally, the vibrational bands in the range of 800–1200 cm^{-1} represent the existence of inorganic compounds. No vibrational band is related to Co − S in Co–SnS_2 nanoplates because the vibrational band of Co − S appears below 400 cm^{-1} [34]. However, the slight shift of the Sn–S vibrational band into lower wavenumbers with doping by cobalt indicates that Co ions are successfully incorporated with SnS_2 nanoplates.

The crystal structure of pure SnS_2 and Co–SnS_2 nanoplates was characterized using XRD patterns (Fig. 2c). The XRD pattern of pure SnS_2 nanoplates exhibits different diffraction peaks at 15.06°, 26.68°, 30.86°, 32.06°, 41.49°, 44.84°, and 48.62° corresponding to diffraction planes of (001), (100), (002), (101), (102), (003), and (110), respectively. This pattern matches with the polycrystalline hexagonal SnS_2 (JCPDS no. 00-023-0677). Other phase appeared in the nanoplates represents the presence of SnS with diffraction planes of (120) and (131) at 22.12° and 39.12°, respectively, according to JCPDS no. 39–0354. The concentration of SnS to SnS_2 in our samples is lower than 7%. SnS_2 illustrates sharp, strong peaks, which is attributed to that the thiourea helps for large crystal growth. The lattice constants (a and c) of SnS_2 crystals are 3.86 Å and 5.79 Å, respectively, which is accepted with the literature [35]. Introducing Co into SnS_2 nanoplates increases the lattice constant a to 3.88 Å. Compared to pure SnS_2 nanoplates, the peak position of Co–SnS_2 nanoplates shifted to lower diffraction angle. For instance, the d-spacing of the (001) plane of Co–SnS_2 is calculated to be 0.592 nm, which is slightly larger than that of pure SnS_2 (0.588 nm). The decreased number of layers and the enlarged inter-layer spacing of Co–SnS_2 could be attributed to the structural strain generated by the expansion of the crystal lattice after the interstitial incorporation of cobalt. According to the Williamson-Hall method, the crystallite size of pure SnS_2 nanoplates is about 25 nm, whereas introducing cobalt into nanoplates increases the crystalline size up to 48 nm.

The optical transmittance measurements of pure SnS_2 and Co–SnS_2 nanoplates were performed (Fig. 3a), followed by calculation the absorption coefficient ($\alpha = (1/d)\ln(1/T)$) and bandgap estimation by Tauc plot (Fig. 3b) [36,37]. The transmittance values of Co–SnS_2 nanoplates in the visible region are lower than those of pure SnS_2 nanoplates. On the other hand, Co–SnS_2 nanoplates exhibit higher absorption coefficient values in the visible region compared to the pure SnS_2 nanoplates. Additionally, the observed indirect bandgap energies of pure SnS_2 and Co–SnS_2 nanoplates are 1.95 and 1.86 eV, respectively, which is accepted in the literature [38,39]. Apparently, doping SnS_2 nanoplates by cobalt creates a microstrain in Co–SnS_2 nanoplates compared to pure SnS_2 nanoplates, affecting the electronic properties of valance and conduction bands (Fig. 3c). The detailed calculations of valance and conduction band energies, as well as the disorder band energy, are described in Supplementary S3. A closer look at Fig. 3c indicates that the valence band position moves from about 1.94 eV for pure SnS_2 nanoplates toward lower energy for Co–SnS_2 nanoplates (~1.83 eV). On the other hand, the conduction band position rises from −0.01 eV for pure SnS_2 nanoplates to −0.03 eV for Co–SnS_2 nanoplates. This is accepted with the strain-induced bandgap transition in bulk SnS_2 [40]. Additionally, the indirect bandgap and additional bands in Co–SnS_2 nanoplates will affect the generation and lifetime of electron-hole pairs, enhancing the charge carrier to participate in

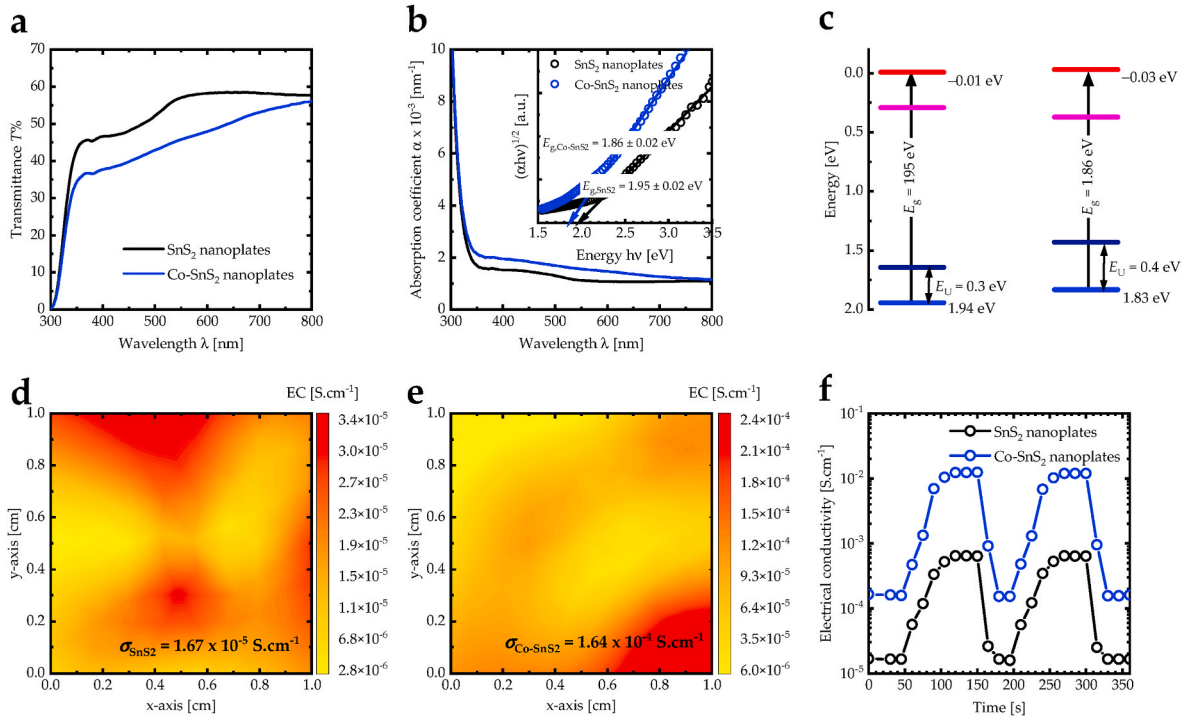

Fig. 3. The optical and Electrical properties of undoped SnS_2 and Co–SnS_2 nanoplates. (a) The transmittance spectra for SnS_2 and Co–SnS_2 nanoplates. (b) The absorption coefficient of SnS_2 and Co–SnS_2 nanoplates. Tauc plots are shown in the inset of the figure presented for calculating the bandgap energies. **(c)** The band structure of SnS2 and Co–SnS2 shows the new valance and conduction bands, and the new configuration of the band structure is revealed by disorder in SnS_2 and Co–SnS_2 nanoplates. **(d, e)** The electrical conductivity scans and the mean electrical conductivity of SnS_2 and Co–SnS_2 nanoplates are in order. **(f)** The photoconductivity of SnS_2 and Co–SnS_2 nanoplates is relevant to the period spent under the UV irradiation.

photocatalyst applications.

The surface morphology reflects the charge distribution disseminated over the film's surface. Keithley multimeter with a 4-point probe was used to investigate the local conductivity on the film's surface to visualize how the charges are distributed at the surface and, hence, how to scan the conductivity in a contour-like charge distribution method. Hence, twelve distinct local points were used as surface-charge distribution focal centers. The electrical conductivity was found at each focal point. The average value was also calculated. A powerful software associated with the system was used to convert the charge distribution over the film's surface, reflecting the conductivity distribution regarding topographic mapping to the charges. The electrical conductivity mapping of the SnS_2 and Co–SnS_2 nanoplates on the surface demonstrate distinct differences associated with the surface morphology variation, as seen in Fig. 3d and e. Moreover, the mean electrical conductivity of SnS_2 nanoplates is 1.67×10^{-5} S.cm^{-1}, which agrees well with the findings in the literature [41]. Doping SnS_2 nanoplates with cobalt increases the electrical conductivity to 1.64×10^{-4} S.cm^{-1}. The enhanced electrical conductivity can be attributed to denoting electrons in the conduction band of SnS_2 by Co atoms, consequently increasing the number of free electrons and the electrical conductivity. Additionally, cobalt atoms act as acceptors that can trap electrons from the valence band, leaving holes in the valence band and consequently increasing the electrical conductivity.

Fig. 3f shows the surface electrical conductivity for the bare SnS_2 and Co–SnS_2 nanoplates evaluated under dark conditions compared to that for the films evaluated under UV light ($\lambda = 260$ nm, 5 W) illumination. The electrical conductivity for the SnS_2 nanoplate surface varies between 1.67×10^{-5} S.cm^{-1} and 6.54×10^{-4} S.cm^{-1} while it varies between 1.64×10^{-4} S.cm^{-1} and 1.25×10^{-2} S.cm^{-1} for the Co–SnS_2 nanoplates, all in an incremental trend. The experiment was repeated several times to ensure a consistent trend and reliability. The morphological charge distribution, and hence the local surface conductivity, demonstrates the production of electron-hole couples caused by the absorption of the U.V. photons by the SnS_2 and Co–SnS_2 surfaces revealing enhanced excited species with more free carriers, and hence, enhanced photoconductivity [42–44]. It is demonstrated in the figure that electrical conductivity enhanced by the photon-film interactions (photoconductivity) for the Co–SnS_2 nanoplates is higher than that for the SnS_2 nanoplates, indicating that incorporating SnS_2 with cobalt boosts the production of charge carriers as a result of composite degradation in the photocatalytic process.

3.2. Photocatalytic degradation analysis

3.2.1. Optimization of the photocatalytic degradation process

The MIT was used to investigate the photocatalytic degradation efficiency of undoped SnS_2 and Co–SnS_2 nanoplates under UV irradiation for 160 min. First, the optimal concentration of MIT for 50 mg/L of nanoplates for the best degradation was explored using various contents of MIT. The absorbance spectra of MIT in relevance to UV-irradiation time after the degradation by SnS_2 and Co–SnS_2 nanoplates with different MIT concentrations are plotted in Supplementary file Figures S3 and S4. The degradation efficiency (*DE*%) of MIT by SnS_2 and Co–SnS_2 nanoplates with different MIT concentrations was found by:

$$DE\% = \left(1 - \frac{A_t}{A_0}\right) \times 100\% \quad (1)$$

Where A_0 and A_t are the cumulative areas under the absorbance band at initial and final periods of UV illumination, respectively (Fig. 4a); the degradation efficiency of Co–SnS_2 nanoplates is higher than that for undoped SnS_2 nanoplates for all the MIT concentrations. This increase is

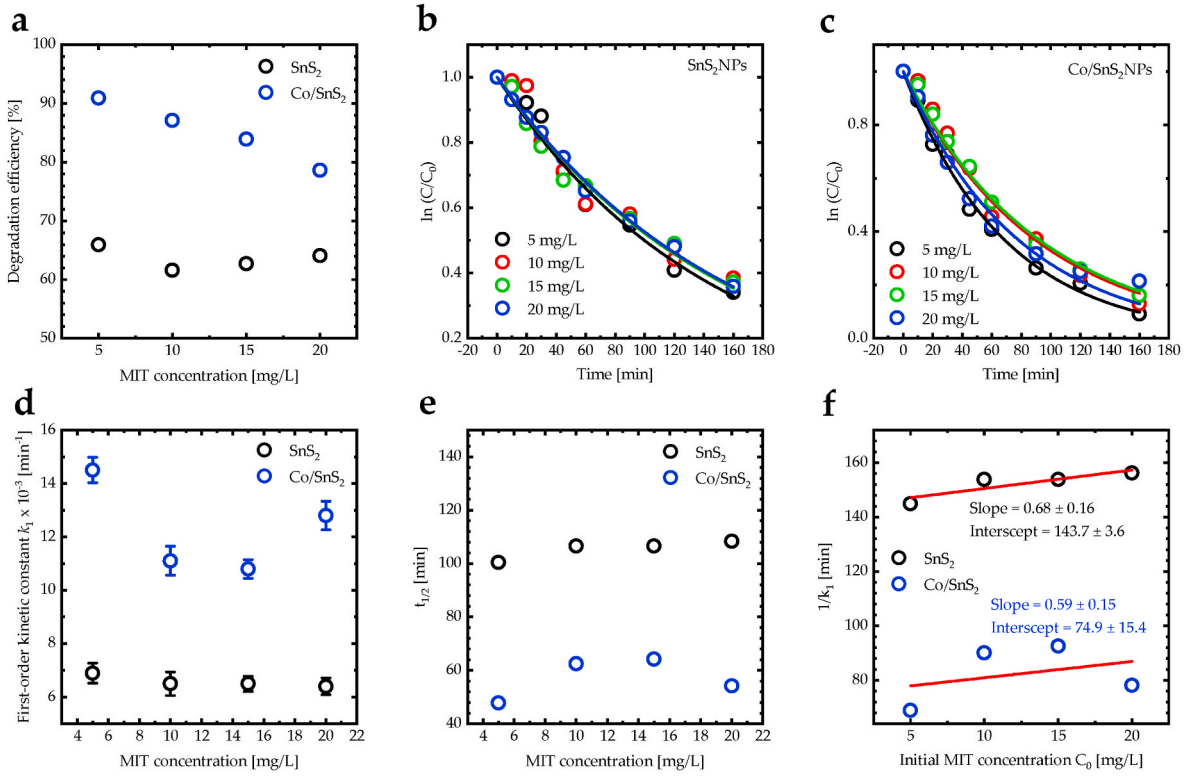

Fig. 4. Photocatalytic degradation analysis of MIT by SnS_2 and Co–SnS_2 nanoplates. (a) The degradation efficiency of MIT by SnS_2 and Co–SnS_2 nanoplates for different MIT concentrations. (b) $\ln(C/C_0)$ of MIT degraded by undoped SnS_2 nanoplates in relevance to the UV-irradiation time. (c) $\ln(C/C_0)$ of MIT degraded by Co–SnS_2 nanoplates in relevance to the UV-irradiation time. (d) The first-ordered kinetic factor k_1 of the degradation development of MIT by SnS_2 and Co–SnS_2 nanoplates for various MIT concentrations. (e) Half-life time of the degradation process of MIT by undoped SnS_2 and Co–SnS_2 nanoplates for different MIT concentrations. (f) Langmuir–Hinshelwood kinetic model: $1/k_1$ of the degradation process of MIT by SnS_2 and Co–SnS_2 nanoplates versus initial MIT concentration.

indorsed due to the reality of incorporating SnS_2 nanoplates with cobalt shrinks energy spacing between the V.B. and C.B. in the energy band structure by the creation of extra recombination sites with low emission energies and producing more $e^- - h^+$ couples leading to more hydroxyl radicals (OH^*) [45]. Additionally, doping SnS_2 nanoplates by Co increases the electrical conductivity of the nanoplates, which increases the electrostatic interactions between the nanoplates and the adsorbed MIT molecules [46].

The higher degradation efficiency of undoped SnS_2 and Co–SnS_2 nanoplates is at 5 mg/L of 66% and 91%, respectively, after 160 min. This can be attributed to many reasons, i.e., introducing Co ions into SnS_2 nanoplates increases the surface area of the nanoplates, decreases the bandgap energy, as well as increases the electrical conductivity and the photoconductivity of the nanoplates. Additionally, according to M. Jiang et al. [47], Co-doped SnS2 nanostructures are chemical and catalysis stable under long-term cycles.

Higher MIT contents reduce the degradation efficiency because MIT molecules accumulate on the nanoplate's surface, forming aggregates of heavy load on the limited number of plates. This heavy load of aggregated MIT molecules masks the nanoplates from the solution, reducing the energetic spots for more interactions and revealing fewer hydroxyl radicals (OH^*) [48]. Additionally, the overconcentration of MIT reduces the depth penetration of UV light through the treated solution, which reduces the surface adsorption to the photons and decreases the generation of hydroxyl radicals (OH^*) [49]. Therefore, the optimal contents of the MIT for 50 mg/L of nanoplates is 5 mg/L.

The photocatalysis degradation effectiveness of SnS_2 and Co–SnS_2 nanoplates was inspected using zero-, first-, and second-ordered kinetic constants (Supplementary file, Figure S5, Table S2). The first-order kinetic reaction is more fit for all MIT concentrations. The first-order kinetic constants (k_1) of SnS_2 and Co–SnS_2 nanoplates were explored by plotting A/A_0 versus the degradation period (Fig. 4b and c) based on Equation S6. The first-order kinetic constant (k_1) is consistent with the degradation efficiency, where the k_1 of Co–SnS_2 nanoplates is higher than SnS_2 nanoplates for all MIT concentrations. The higher k_1 of undoped SnS_2 and Co–SnS_2 nanoplates is at 5 mg/L of 6.9×10^{-3} and 14.5×10^{-3}, respectively (Fig. 4d). The half-life time of the degradation development of MIT by SnS_2 and Co–SnS_2 nanoplates is calculated using $t_{1/2} = \ln 2/k_1$. The half-life time of the degradation process of MIT by Co–SnS_2 nanoplates is lower than that of undoped SnS_2 nanoplates. The lower $t_{1/2}$ of undoped SnS_2 and Co–SnS_2 nanoplates is at 5 mg/L for about 100 and 48 min, respectively (Fig. 4e).

The adsorption factor at equilibrium (K_L) and the kinetic rate constraints of the plate's surface interaction (k_s) were modulated by Langmuir–Hinshelwood formula (equation (2)) via manipulating the plots of the reciprocal first-order kinetic factor ($1/k_1$) against the primary contents (C_0) of the MIT (Fig. 4f) [50],

$$\frac{1}{k_1} = \frac{1}{K_L k_s} + \frac{C_0}{k_s} \tag{2}$$

The K_L of SnS_2 and Co–SnS_2 nanoplates is 0.005 and 0.008 $(mgL^{-1})^{-1}$, and the k_s of SnS_2 and Co–SnS_2 nanoplates is 1.47 and 1.69 $mgL^{-1}.min^{-1}$. These outcomes designate that Co–SnS_2 nanoplates have a higher adsorption rate of MIT molecules than SnS_2 nanoplates.

3.2.2. Analysis of MIT photocatalytic degradation

Based on the outcomes found in the preceding part of this work, the highest *DE*% and k_1 were found for 5 mg/L of MIT at 50 mg/L contents of Co–SnS_2 nanoplates. In this section, we will investigate the photocatalytic degradation pathway of MIT molecules by analyzing MIT's UV–Vis and FTIR spectra evolution that was photodegraded using Co–SnS_2 nanoplates. First, the UV–Vis absorbance spectra evolution of MIT aqueous solution for different photocatalytic degradation times is plotted in Fig. 5a. The primary peak response for the MIT absorption by UV illumination in the composite solution was found at 274.0 nm,

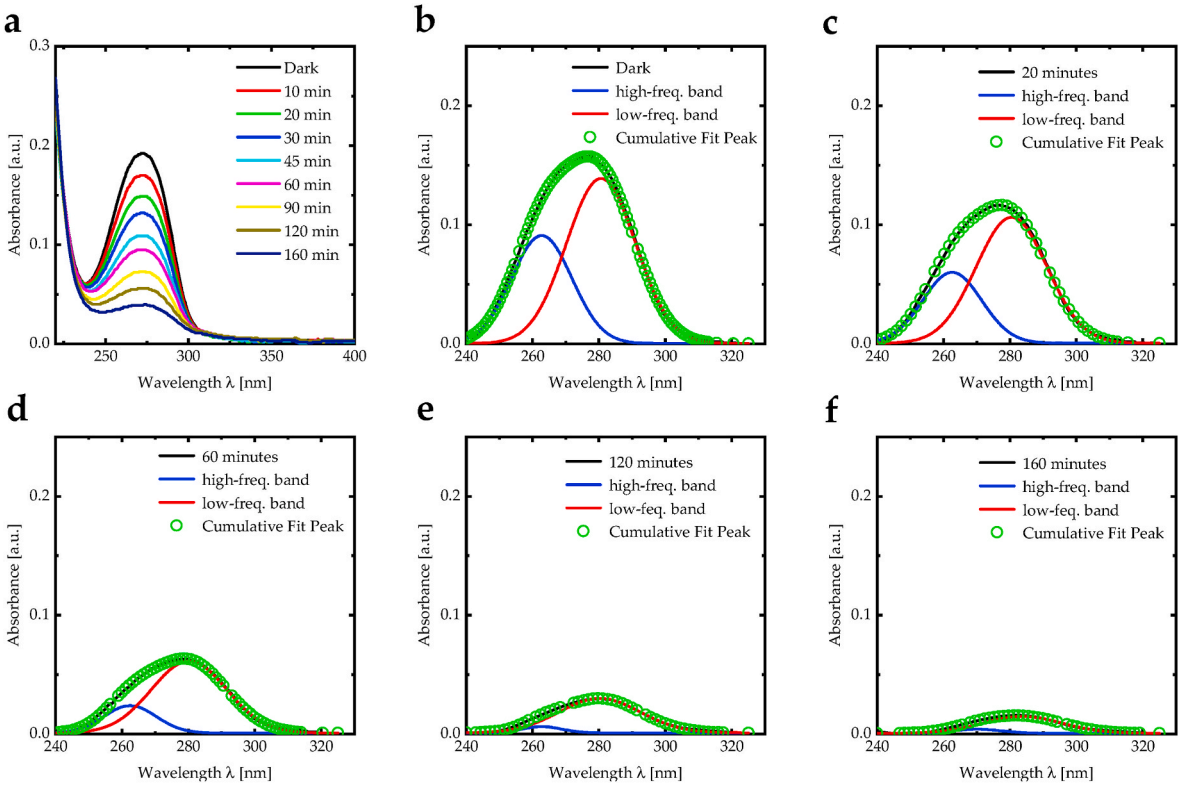

Fig. 5. Analysis of the MIT absorption spectra growth. (a) The absorbance spectra growth for the MIT is relevant to the UV-illumination period beyond the degradation process by 50 mg/L of Co–SnS_2 nanoplates in an initial MIT content of 5 mg/L. The Gaussian function fitting peaks for the main absorbance peak of MIT for the photocatalysis developing periods are (b) 0 min, (c) 20 min, (d) 60 min, (e) 120 min, and (f) 160 min.

forming an under-curve area of 5.70 and a main full linewidth of 29.45. The absorption response curve for the MIT molecules decays by increasing the period of the UV irradiation to form an absorbance band with a peak at 281.7 nm with an under-curve area of 0.48 and main full linewidth of 25.8, revealing a most degrading time to be 160 min with a *DE*% of around 91%.

The absorption curve-trend for the MIT becomes more convoluted by increasing the photocatalytic dispossession period. The drop in the absorption curve-trend by more prolonged UV exposure proposes that the main absorption band encompasses two sup-absorption frequencies that are influenced separately by the photocatalytic degradation periods. According to Shirley's analysis technique, a base reference line was first made for manipulating the absorption peak [51]. Various curve-fitting approaches to find the best outreach results include two Gaussian curves fitting, Voigt, bi-Gaussian, and log-normal distribution functions. Gaussian curve-fitting was the greatest treatment for our experimental data over the whole range of the wavelengths with an average square root R^2 of 0.99 as it best fits the dye absorption bands [52–54]. Hence, the absorption bands were fitted to double Gaussian peaks between 240 and 320 nm, as seen in Fig. 5b–f.

The main absorbance band comprised two sub-bands: a high-frequency band with an absorption peak of 262.7 nm and band area of 2.07 a.u. and a low-frequency band with an absorption peak of 280.6 nm and band area of 3.63 a.u. (Fig. 5b). The UV irradiation period influences each sub-band's peak position, area, and linewidth differently (Fig. 5c–f). The two sub-bands The area shows a similar cur-trend as that for the main MIT absorbance band-trend (Figure S6a), demonstrating that the degradation process occurs throughout the composite platform of the Co–SnS_2 nanoplates and the MIT molecules. The degradation process reveals hypsochromic coupling indicated by the absorption peak's red shifting. The high-frequency band acquired considerable red shifting behaviour from 262.7 nm to 270.1 nm, while the low-frequency peak shifted slightly from 280.6 nm to 283.7 nm. The influence of U.V. irradiation on catalytic degradation indicates that the process reveals a tendency to reach lower energy by such a hypsochromic interaction where MIT molecules serve as hydrogen acceptors while producing hydroxides from the photo-oxidation process (Figure S6b) [55]. The variation in the absorption band's behaviour reflects various interactions that may have occurred during the catalytic degradation process, including hydrophobic/hydrophilic and dipole-dipole interactions based on the role of the hydrogen interaction [56].

The photocatalytic degradation process produces hydroxyl radicals due to the role of hydrogen bonding interactions. Hence, acidity level (pH) is correlated to the production of hydroxyls. The pH is shown to increase from 5.11 to 7.24 while the electrical conductivity declines linearly from 118.0 μS cm^{-1} to 59.2 μS cm^{-1} as the period of the UV-illumination increases from 0 to 160 min (Figure S7). Increasing linearly the pH level while decreasing the electrical conductivity as a function of the UV-illumination period shows that the degradation process is dominant by the role of hydrogen bonding interactions. In contrast, ionic interactions do not affect the process. However, the hydroxyl radicals and hydronium ions have mutual interactions and consequently terminate the activation of the MIT molecules away from ionic interactions.

Based on the above discussion, FTIR spectra analyses (Supplementary file, Figure S5) were used to investigate the possible MIT degradation pathway. The MIT can be degraded with two degradation pathways (Fig. 6), as reported in the R. Ren et al. study [13]. The first pathway contains five stages, whereas the second one contains two. In the first pathway, the hydroxyl radicals (OH^*) interact with the electron-rich double-bonded MIT, forming 4,5-dihydroxy-2-methylisothiazolidin-3-one. After that, oxygen interacts with the hydroxyl groups, forming 2-methylisothiazolidine-3,4,5-trione. Subsequently, several interactions were performed with 2-methylisothiazolidine-3,4,5-trione, forming 2,2-dihydroxy-2-(mercapto(methyl)amino)acetic acid.

On the other hand, the second pathway involves direct oxidation of MIT molecules by undoped SnS_2 and Co–SnS_2 nanoplates, leading to the cleaving of the carbon-carbon double bond in the heterocyclic ring of MIT, forming 2-(dimethylamino)-2,2-dihydroxyacetic acid. Subsequent removal of a methyl group from 2-(dimethylamino)-2,2-dihydroxyacetic acid gives rise to N-mercapto-N-methylacetamide. The final products in the two pathways undergo further mineralization, ultimately forming CO_2 and H_2O.

3.2.2.1. Photocatalytic degradation process. The optical chemo-mechanism of the photocatalytic degradation process occurs between the semiconductor and the organic molecules under UV illumination, as in the following scenario. The organic molecules of the MIT are initially adsorbed at the surface of SnS_2 and Co–SnS_2 nanoplates [57]. The semiconductors (SnS_2 and Co–SnS_2) are motivated by UV illumination, causing a generation of free carriers ($e^- - h^+$ in pairs. Electrons are then captured by surrounding oxygen (O_2), producing superoxide radicals (O_2^{-*}). In the meantime, holes interact with water molecules (H_2O) to produce hydroxyl radicals (OH^*) as seen in Fig. 7 [58]. The free radicals react with the organic molecules, destroying the MIT strong coupling bonds and, hence, degrade by the adsorption process to the semiconductor surface [59].

3.2.2.2. Consumption of electrical energy. The energy consumed by the

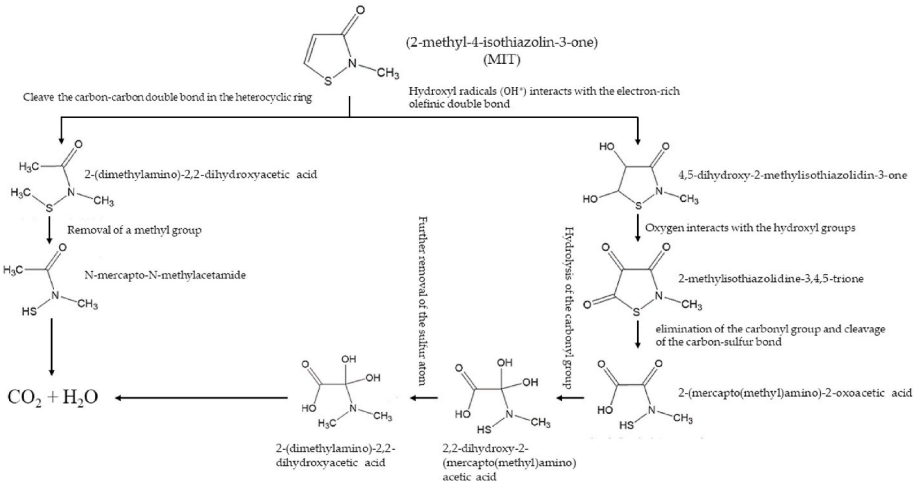

Fig. 6. Established degradation pathway of MIT.

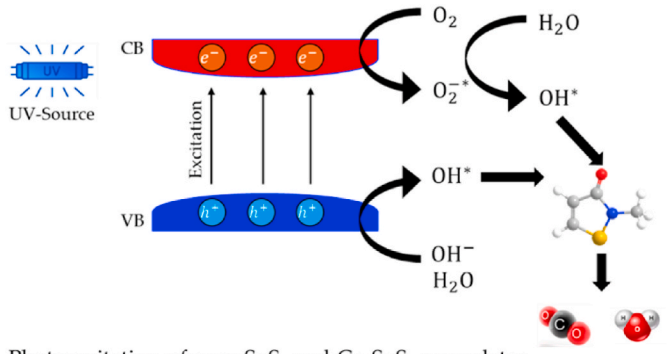

Photoexcitation of pure SnS_2 and Co-SnS_2 nanoplates

$$SnS_2\,(Co - SnS_2) + h\nu \rightarrow e^- + h^+$$

Ionosorption of adsorbed oxygen

$$e^- + O_2 \rightarrow O_2^{-*}$$

Water ionization

$$h^+ + H_2O \rightarrow H^+ + OH^*$$

Oxidation of hydroxyl ions by h^+

$$h^+ + OH^- \rightarrow OH^*$$

Degradation of organic molecules by active species

$$OH^- + OH^* + \text{Org. Mol} \rightarrow CO_2 + H_2O$$

Fig. 7. The schematic illustration of the scheme of the photo degradation process by SnS_2 and Co–SnS_2 nanoplates under UV irradiation.

reaction of the photocatalytic degradation process is defined by the electric energy consumed/order (E_{EO}) kilowatt-hours (kWh) needed to extract a named contaminant per first order of magnitude (90%) per 1-m cube of polluted water. E_{EO} is defined by Ref. [60]:

$$E_{EO} = \frac{1000Pt}{60V\ln\left(\frac{C_o}{C_f}\right)} \quad (3)$$

where E_{EO} is the electric energy per order (kWh/m^3); P is the nominal power of the light source (kW) (16 W); t is the irradiation time (minutes) (160 min); C_0 and C_f are the MIT initial and final concentrations (mg/L), and V is the solution volume (0.05 L). The electrical energy consumption of Co–SnS_2 nanoplates is 356 kWh/m^3, which is lower than that of undoped SnS_2 nanoplates (793 kWh/m^3). This means using Co–SnS_2 nanoplates requires about half the electric energy used in undoped SnS_2 nanoplates. A research study has investigated the photocatalytic degradation of MIT using a TiO_2NPs/persulfate system under simulated solar irradiation. P. Gómez-Rodríguez et al. [12] successfully decomposed the MIT using TiO_2NPs/persulfate system under a 1500 W Xenon lamp ($\lambda < 300$ nm). Their system's calculated electrical energy consumption is about 650 kWh/m^3, meaning that our system (Co–SnS_2 nanoplates) requires lower electric energy in the TiO_2NPs/persulfate system.

4. Conclusions

In this work, the degradation of MIT in water under U.V. irradiation was investigated with undoped SnS_2 and Co–SnS_2 nanoplates synthesized by a hydrothermal method at 180 °C. Fourier transform infrared and energy-dispersive X-ray spectroscopies were confirmed to be successfully incorporated for Co with SnS_2 nanoplates. On the other hand, X-ray diffraction patterns show that the crystallite size of nanoplates increases from 26 nm to 48 nm. Undoped SnS_2 nanoplates exhibit plate-like nanostructure with smooth surfaces, with a size of 150–400 μm and a 50–70 nm thickness. Doping SnS_2 nanoplates with cobalt increases the nanoplate's size to 300–600 nm. Undoped SnS_2 and Co–SnS_2 nanoplates have indirect bandgap energy with values of 1.95 and 1.86 eV, respectively. On the other hand, the electrical conductivity of undoped SnS_2 and Co–SnS_2 nanoplates is 1.67×10^{-5} S.cm^{-1} and 1.64×10^{-4} S.cm^{-1}, respectively. The degradation efficiency of Co–SnS_2 nanoplates is higher than undoped SnS_2 nanoplates for all MIT concentrations. The higher degradation efficiency of undoped SnS_2 and Co–SnS_2 nanoplates after 160 min is at 5 mg/L of 66% and 91%, respectively. The higher k_1 of undoped SnS_2 and Co–SnS_2 nanoplates is at 5 mg/L of 6.9×10^{-3} and 14.5×10^{-3}, respectively. The adsorption equilibrium constant (K_L) of undoped SnS_2 and Co–SnS_2 nanoplates is 0.005 and 0.008 (mgL^{-1})$^{-1}$, and the kinetic rate constant of the surface reaction (k_s) of undoped SnS_2 and Co–SnS_2 nanoplates is 1.47 and 1.69 mgL^{-1}.min^{-1}. These results indicate that Co–SnS_2 nanoplates have higher adsorption of MIT molecules than undoped SnS_2 nanoplates. The electrical energy consumption of Co–SnS_2 nanoplates is 356 kWh/m^3, which is lower than in undoped SnS_2 nanoplates (793 kWh/m^3). This means using Co–SnS_2 nanoplates requires about half the electric energy used in undoped SnS_2 nanoplates. To conclude, according to the previous discussion, this research may pave the way for the further design of SnS_2-based photocatalysts in enhancing the photocatalytic activity of organic materials degradation.

Consent to participate

All authors participate in this work.

Consent to publish

All authors agree to publish this work.

CRediT authorship contribution statement

Qais M. Al-Bataineh: Writing – original draft, Visualization, Software, Methodology, Investigation, Formal analysis, Conceptualization. **A.B. Migdadi:** Writing – original draft, Visualization, Software, Methodology, Investigation, Formal analysis, Conceptualization. **Ahmad A. Ahmad:** Writing – original draft, Validation, Supervision, Resources, Project administration, Formal analysis, Data curation, Conceptualization. **Oana Brincoveanu:** Writing – review & editing, Validation, Resources. **Alexandra Mocanu:** Writing – review & editing, Validation, Software, Investigation. **Gabriela Toader:** Writing – review & editing, Validation, Investigation. **Ahmad D. Telfah:** Writing – review & editing, Validation, Supervision, Project administration, Methodology, Data curation.

Declaration of competing interest

The authors declare that they have no known competing financial interests or personal relationships that could have appeared to influence the work reported in this paper.

Data availability

Data will be made available on request.

Acknowledgement

The scientific support provided by the Ministerium für Innovation, Wissenschaft und Forschung des Landes Nordrhein-Westfalen, the Senatsverwaltung für Wirtschaft, Technologie und Forschung des Landes Berlin, and the Bundesministerium für Bildung und Forschung is sincerely appreciated. The authors extend their gratitude to Jordan University of Science and Technology. Additionally, we would like to thank Prof. Mohammad-Ali H. Al-Akhras for his invaluable assistance in facilitating our team members' use of the biomedical laboratory.

Appendix A. Supplementary data

Supplementary data to this article can be found online at https://doi.org/10.1016/j.matchemphys.2024.129184.

References

[1] A.A. Ahmad, Q.M. Al-Bataineh, I.A. Aljarrah, A.D. Telfah, Electrochemical degradation of methyl red in zinc hydroxide and zinc oxide thin films, physical and chemical activation, Mater. Chem. Phys. 280 (2022) 125793.

[2] J. Zhou, et al., A novel PN heterojunction with staggered energy level based on ZnFe2O4 decorating SnS2 nanosheet for efficient photocatalytic degradation, Appl. Surf. Sci. 510 (2020) 145442.

[3] P. Singh, et al., Systematic review on applicability of magnetic iron oxides–integrated photocatalysts for degradation of organic pollutants in water, Mater. Today Chem. 14 (2019) 100186.

[4] S. Sharma, et al., Carbon quantum dot supported semiconductor photocatalysts for efficient degradation of organic pollutants in water: a review, J. Clean. Prod. 228 (2019) 755–769.

[5] T. Wang, et al., Synthesis of redox-mediator-free direct Z-scheme AgI/WO3 nanocomposite photocatalysts for the degradation of tetracycline with enhanced photocatalytic activity, Chem. Eng. J. 300 (2016) 280–290.

[6] X.-j. Chen, Y.-z. Dai, X.-y. Wang, J. Guo, T.-h. Liu, F.-f. Li, Synthesis and characterization of Ag3PO4 immobilized with graphene oxide (GO) for enhanced photocatalytic activity and stability over 2, 4-dichlorophenol under visible light irradiation, J. Hazard Mater. 292 (2015) 9–18.

[7] S. Kresmann, A.H.R. Arokia, C. Koch, B. Sures, Ecotoxicological potential of the biocides terbutryn, octhilinone and methylisothiazolinone: underestimated risk from biocidal pathways? Sci. Total Environ. 625 (2018) 900–908.

[8] R. Nagorka, C. Gleue, C. Scheller, H.J. Moriske, W. Straff, Isothiazolone emissions from building products, Indoor Air 25 (1) (2015) 68–78.

[9] S.-K. Park, J.-H. Kwon, The fate of two isothiazolinone biocides, 5-chloro-2-methylisothiazol-3 (2H)-one (CMI) and 2-methylisothiazol-3 (2H)-one (MI), in liquid air fresheners and assessment of inhalation exposure, Chemosphere 144 (2016) 2270–2276.

[10] Y. Wang, et al., Electrochemical degradation of methylisothiazolinone by using Ti/SnO2-Sb2O3/α, β-PbO2 electrode: kinetics, energy efficiency, oxidation mechanism and degradation pathway, Chem. Eng. J. 374 (2019) 626–636.

[11] N. Huang, et al., Removal of methylisothiazolinone biocide from wastewater by VUV/UV advanced oxidation process: kinetics, mechanisms and toxicity, J. Environ. Manag. 315 (2022) 115107.

[12] P. Gómez-Rodríguez, P. Calza, D. Fabbri, C. Medana, R. van-Grieken, M.-J. López-Muñoz, Photocatalytic degradation of methylisothiazolinone in water by TiO2 and TiO2/persulfate systems with simulated solar radiation, Catal. Today 413 (2023) 113942.

[13] R. Ren, et al., Indirect oxidation mechanism governing in P-rGO/Ti anode with C2-PO2/rGO configuration for efficient 2-Methyl-4-Isothiazolin-3-one electrooxidation, Chem. Eng. J. 461 (2023) 141934.

[14] I. Shown, et al., Carbon-doped SnS2 nanostructure as a high-efficiency solar fuel catalyst under visible light, Nat. Commun. 9 (1) (2018) 169.

[15] Y.C. Zhang, Z.N. Du, K.W. Li, M. Zhang, Size-controlled hydrothermal synthesis of SnS2 nanoparticles with high performance in visible light-driven photocatalytic degradation of aqueous methyl orange, Separ. Purif. Technol. 81 (1) (2011) 101–107.

[16] Y. Liu, et al., In-situ fabrication SnO2/SnS2 heterostructure for boosting the photocatalytic degradation of pollutants, Chin. J. Catal. 41 (10) (2020) 1554–1563.

[17] M. Bryushinin, G. Dubrovsky, I. Sokolov, Non-steady-state photocurrents in SnS2 crystals, Appl. Phys. B 68 (1999) 871–875.

[18] X. Zhou, Q. Zhang, L. Gan, H. Li, T. Zhai, Large-size growth of ultrathin SnS2 nanosheets and high performance for phototransistors, Adv. Funct. Mater. 26 (24) (2016) 4405–4413.

[19] J.Z. Ou, et al., Physisorption-based charge transfer in two-dimensional SnS2 for selective and reversible NO2 gas sensing, ACS Nano 9 (10) (2015) 10313–10323.

[20] B. Yang, et al., SnS2 as low-cost counter-electrode materials for dye-sensitized solar cells, Mater. Lett. 133 (2014) 197–199.

[21] C. Ma, et al., Investigating the energy storage mechanism of SnS2-rGO composite anode for advanced Na-ion batteries, Chem. Mater. 27 (16) (2015) 5633–5640.

[22] T. Feng, et al., SnS2 nanosheets for Er-doped fiber lasers, ACS Appl. Nano Mater. 3 (1) (2019) 674–681.

[23] R. Lather, P. Jeevanandam, Synthesis of Zn2+ doped SnS2 nanoparticles using a novel thermal decomposition approach and their application as adsorbent, J. Alloys Compd. 891 (2022) 161989.

[24] D. Voiry, J. Yang, M. Chhowalla, Recent strategies for improving the catalytic activity of 2D TMD nanosheets toward the hydrogen evolution reaction, Adv. Mater. 28 (29) (2016) 6197–6206.

[25] A.K. Singh, K. Mathew, H.L. Zhuang, R.G. Hennig, Computational screening of 2D materials for photocatalysis, J. Phys. Chem. Lett. 6 (6) (2015) 1087–1098.

[26] D. Prabha, et al., Spectroscopic, magnetic and antibacterial properties of Sr-doped SnS2 nanopowders, Optik 142 (2017) 301–310.

[27] R. Lather, P. Jeevanandam, Novel thermal decomposition method for the synthesis of iron-doped SnS2 nanoparticles and studies on their peroxidase-like activity, ChemNanoMat 8 (6) (2022) e202200036.

[28] Y. Liu, et al., Cu doped SnS2 nanostructure induced sulfur vacancy towards boosted photocatalytic hydrogen evolution, Chem. Eng. J. 407 (2021) 127180.

[29] R. Bairy, P. shankaragouda Patil, S.R. Maidur, H. Vijeth, M. Murari, U. Bhat, The role of cobalt doping in tuning the band gap, surface morphology and third-order optical nonlinearities of ZnO nanostructures for NLO device applications, RSC Adv. 9 (39) (2019) 22302–22312.

[30] S. Chakma, V.S. Moholkar, Investigation in mechanistic issues of sonocatalysis and sonophotocatalysis using pure and doped photocatalysts, Ultrason. Sonochem. 22 (2015) 287–299.

[31] J.-H. Park, J.C. Ro, S.-J. Suh, Facile synthesis of Co-doped SnS2 as a pre-catalyst for efficient oxygen evolution reaction, Curr. Appl. Phys. 42 (2022) 50–59.

[32] J. Srivind, et al., Visible light irradiated photocatalytic and magnetic properties of Fe-doped SnS 2 nanopowders, J. Mater. Sci. Mater. Electron. 29 (2018) 9016–9024.

[33] T. Lastovina, et al., Solvothermal synthesis of Sm3+-doped Fe3O4 nanoparticles, Mater. Sci. Eng. C 80 (2017) 110–116.

[34] X. Meng, J. Deng, J. Zhu, H. Bi, E. Kan, X. Wang, Cobalt sulfide/graphene composite hydrogel as electrode for high-performance pseudocapacitors, Sci. Rep. 6 (1) (2016) 21717.

[35] M. Amroun, M. Khadraoui, Effect of substrate temperature on the properties of SnS2 thin films, Optik 184 (2019) 16–27.

[36] A.A. Ahmad, M.H. Khazaleh, A.M. Alsaad, Q.M. Al-Bataineh, A.D. Telfah, Characterization of As-prepared PVA-PEO/ZnO-Al2O3-NPs hybrid nanocomposite thin films, Polym. Bull. 79 (11) (2022) 9881–9905.

[37] I. Dhahri, et al., Optical and structural properties of ZnO NPs and ZnO–Bi2O3 nanocomposites, Ceram. Int. 48 (1) (2022) 266–277.

[38] B. Sainbileg, M. Hayashi, Possible indirect to direct bandgap transition in SnS2 via nickel doping, Chem. Phys. 522 (2019) 59–64.

[39] K. Sharma, et al., Strategies and perspectives of tailored SnS2 photocatalyst for solar driven energy applications, Sol. Energy 231 (2022) 546–565.

[40] B. Ram, A.K. Singh, Strain-induced indirect-to-direct band-gap transition in bulk SnS 2, Phys. Rev. B 95 (7) (2017) 075134.

[41] K. Kourtakis, J. DiCarlo, R. Kershaw, K. Dwight, A. Wold, Preparation and characterization of SnS2, J. Solid State Chem. 76 (1) (1988) 186–191.

[42] S.F. Akhtarianfar, A. Khayatian, R. Shakernejad, M. Almasi-Kashi, S.W. Hong, Improved sensitivity of UV sensors in hierarchically structured arrays of network-loaded ZnO nanorods via optimization techniques, RSC Adv. 7 (51) (2017) 32316–32326.

[43] A.A. Ahmad, A. Migdadi, A.M. Alsaad, I. Qattan, Q.M. Al-Bataineh, A. Telfah, Computational and experimental characterizations of annealed Cu2ZnSnS4 thin films, Heliyon 8 (1) (2022) e08683.

[44] A. Ahmad, A. Migdadi, A. Alsaad, Q.M. Al-Bataineh, A. Telfah, Optical, structural, and morphological characterizations of synthesized (Cd–Ni) co-doped ZnO thin films, Appl. Phys. A 127 (12) (2021) 922.

[45] I.Y.-Y. Bu, Sol-gel synthesis of p-type zinc oxide using potassium permanganate, Optik 179 (2019) 259–265.

[46] Y.-H. Chiu, T.-F.M. Chang, C.-Y. Chen, M. Sone, Y.-J. Hsu, Mechanistic insights into photodegradation of organic dyes using heterostructure photocatalysts, Catalysts 9 (5) (2019) 430.

[47] M. Jiang, Y. Huang, W. Sun, X. Zhang, Co-doped SnS 2 nanosheet array for efficient oxygen evolution reaction electrocatalyst, J. Mater. Sci. 54 (2019) 13715–13723.

[48] P. Velusamy, S. Pitchaimuthu, S. Rajalakshmi, N. Kannan, Modification of the photocatalytic activity of TiO2 by β-Cyclodextrin in decoloration of ethyl violet dye, J. Adv. Res. 5 (1) (2014) 19–25.

[49] M. Faraz, F.K. Naqvi, M. Shakir, N. Khare, Synthesis of samarium-doped zinc oxide nanoparticles with improved photocatalytic performance and recyclability under visible light irradiation, New J. Chem. 42 (3) (2018) 2295–2305.

[50] A. Migdadi, M. Alqadi, F. Alzoubi, H. Al-Khateeb, W.T. Bani-Hani, Photocatalytic activity of prepared ZnO/CuO nanocomposites and kinetic degradation study of methylene blue, J. Mater. Sci. Mater. Electron. 33 (36) (2022) 26744–26763.

[51] R. Murakami, et al., Background estimation in X-ray photoelectron spectroscopy data using an active Shirley method with automated selection of the analytical range, e-J. Surf. Sci. Nanotechnol. 17 (2019) 61–68.

[52] A. Alsaad, Q.M. Al-Bataineh, M. Telfah, A. Ahmad, Z. Albataineh, A. Telfah, Optical properties and photo-isomerization processes of PMMA–BDK–MR nanocomposite thin films doped by silica nanoparticles, Polym. Bull. 78 (2021) 3425–3441.

[53] Q.M. Al-Bataineh, A. Ahmad, A. Alsaad, I. Qattan, A.A. Bani-Salameh, A.D. Telfah, Kinematics of photoisomerization processes of PMMA-BDK-MR polymer composite thin films, Polymers 12 (6) (2020) 1275.

[54] Q.M. Al-Bataineh, A.A. Ahmad, A.M. Alsaad, A. Telfah, New insight on photoisomerization kinetics of photo-switchable thin films based on azobenzene/graphene hybrid additives in polyethylene oxide, Polymers 12 (12) (2020) 2954.

[55] A.S. Özen, P. Doruker, V. Aviyente, Effect of cooperative hydrogen bonding in azo− hydrazone tautomerism of azo dyes, J. Phys. Chem. 111 (51) (2007) 13506–13514.

[56] Q.M. Al-Bataineh, W.T. Bani-Hani, A.A. Ahmad, A.M. Alsaad, A.D. Telfah, Promising electrochemical catalytic steel electrodes structure coated by ZnO films for water treatment and water-splitting applications, J. Mater. Sci. Mater. Electron. (2022) 1–11.

[57] C.-H. Wu, J.-M. Chern, Kinetics of photocatalytic decomposition of methylene blue, Ind. Eng. Chem. Res. 45 (19) (2006) 6450–6457.

[58] M. Kuru, H. Narsat, The effect of heat treatment temperature and Mg doping on structural and photocatalytic activity of ZnO thin films fabricated by RF magnetron co-sputtering technique, J. Mater. Sci. Mater. Electron. 30 (2019) 18484–18495.
[59] F. Bureš, Fundamental aspects of property tuning in push–pull molecules, RSC Adv. 4 (102) (2014) 58826–58851.
[60] J. R. Bolton, K. G. Bircher, W. Tumas, and C. A. Tolman, Figures-of-merit for the technical development and application of advanced oxidation technologies for both electric-and solar-driven systems (IUPAC Technical Report), Pure Appl. Chem. 73 (4) (2001) 627–637.